A&A 612, A27 (2018)
https://doi.org/10.1051/0004-6361/201732284

Astronomy & Astrophysics

The hypersoft state of Cygnus X–3

A key to jet quenching in X-ray binaries?

K. I. I. Koljonen[1,2], T. Maccarone[3], M. L. McCollough[4], M. Gurwell[4], S. A. Trushkin[5,6], G. G. Pooley[7], G. Piano[8], and M. Tavani[8,9,10]

[1] Finnish Centre for Astronomy with ESO (FINCA), University of Turku, Väisäläntie 20, 21500 Piikkiö, Finland
e-mail: karri.koljonen@utu.fi
[2] Aalto University Metsähovi Radio Observatory, PO Box 13000, 00076 Aalto, Finland
[3] Department of Physics and Astronomy, Texas Tech University, Box 41051, Lubbock, TX 79409-1051, USA
[4] Harvard-Smithsonian Center for Astrophysics, Cambridge, MA 02138, USA
[5] Special Astrophysical Observatory RAS, Nizhnij Arkhyz 369167, Russia
[6] Kazan Federal University, Kazan, 420008, Russia
[7] University of Cambridge, Astrophysics, Cavendish Laboratory, Cambridge CB3 0HE, UK
[8] INAF-IAPS, Via del Fosso del Cavaliere 100, 00133 Roma, Italy
[9] INFN Roma Tor Vergata, Via della Ricerca Scientifica 1, 00133 Roma, Italy
[10] Dipartimento di Fisica, Università di Roma "Tor Vergata", Via Orazio Raimondo 18, 00173 Roma, Italy

Received 13 November 2017 / Accepted 21 December 2017

ABSTRACT

Context. Cygnus X–3 is a unique microquasar in the Galaxy hosting a Wolf-Rayet companion orbiting a compact object that most likely is a low-mass black hole. The unique source properties are likely due to the interaction of the compact object with the heavy stellar wind of the companion.
Aims. In this paper, we concentrate on a very specific period of time prior to the massive outbursts observed from the source. During this period, Cygnus X–3 is in a so-called hypersoft state, in which the radio and hard X-ray fluxes are found to be at their lowest values (or non-detected), the soft X-ray flux is at its highest values, and sporadic γ-ray emission is observed. We use multiwavelength observations to study the nature of the hypersoft state.
Methods. We observed Cygnus X–3 during the hypersoft state with *Swift* and *NuSTAR* in X-rays and SMA, AMI-LA, and RATAN-600 in the radio. We also considered X-ray monitoring data from MAXI and γ-ray monitoring data from AGILE and *Fermi*.
Results. We found that the spectra and timing properties of the multiwavelength observations can be explained by a scenario in which the jet production is turned off or highly diminished in the hypersoft state and the missing jet pressure allows the wind to refill the region close to the black hole. The results provide proof of actual jet quenching in soft states of X-ray binaries.

Key words. accretion, accretion disks – binaries: close – stars: individual: Cyg X–3 – stars: winds, outflows – X-rays: binaries

1. Introduction

Cygnus X–3 (Cyg X–3) is a unique X-ray binary (XRB) in the Galaxy hosting a Wolf-Rayet (WR) companion orbiting a compact object (van Kerkwijk et al. 1992; Koljonen & Maccarone 2017). It is a persistent, bright source at radio and X-ray wavelengths, featuring radio flux density levels around 100 mJy (e.g., Waltman et al. 1994) and $2-8\times10^{-8}$ erg cm^{-2} s^{-1} bolometric X-ray flux (e.g., Hjalmarsdotter et al. 2008) ~50% of the time. For a distance estimate of 7.4 kpc (McCollough et al. 2016) these correspond to luminosities 10^{31}–10^{32} erg s^{-1} and $1–5\times10^{38}$ erg s^{-1}, respectively; for the second best distance solution of 10.2 kpc the luminosities are a factor of two higher (see McCollough et al. 2016 for details on the distance estimation). Occasionally, Cyg X–3 undergoes giant radio outbursts, during which the radio flux density levels can reach 20 Jy (Waltman et al. 1996) making Cyg X–3 the brightest Galactic radio source. During the outbursts, a one-sided relativistic jet with multiple knots has been resolved with Very Long Baseline Interferometry (VLBI; Mioduszewski et al. 2001; Miller-Jones et al. 2004; Tudose et al. 2007). The jet morphology implies that the jet axis lies close to our line of sight (<14 degrees; Mioduszewski et al. 2001; Miller-Jones et al. 2009). Contrary to other XRBs, these outbursts are seen when the source makes transitions from the soft state to the hard state (Szostek et al. 2008; Koljonen et al. 2010). The outbursts are preceded by a radio quiet period (down to ~1 mJy; Waltman et al. 1996; Fender et al. 1997; Koljonen et al. 2010), where the X-ray spectra are found to be at their softest (so-called hypersoft state; Koljonen et al. 2010). γ-ray emission is most often detected from Cyg X–3 when the source is transiting to/from the hypersoft state, and on occasion during the hypersoft state when connected to minor radio flaring episodes (Tavani et al. 2009b; Fermi LAT Collaboration et al. 2009; Corbel et al. 2012; Bulgarelli et al. 2012). It has been suggested that the unique source properties, namely the peculiar X-ray spectra and γ-ray emission, are due to the short orbital separation ($2-3\times10^{11}$ cm) coupled with the interaction of the compact object with the high-density stellar wind and photon field ($L_{WR}\sim4-6\times10^{38}$ erg s^{-1}) of the WR companion where the compact object is embedded (Paerels et al. 2000; Szostek & Zdziarski 2008; Zdziarski et al. 2010; Dubus et al. 2010; Piano et al. 2012; Zdziarski et al. 2012).

Previously, a similar X-ray spectrum that was defined as hypersoft state spectrum in Koljonen et al. (2010) was observed from Cyg X–3 in Smale et al. (1993) using the Broad-Band X-ray Telescope, in Beckmann et al. (2007) using the International γ-Ray Astrophysics Laboratory, and in Szostek & Zdziarski (2005) using the *BeppoSAX* satellite. This state is characterized, firstly, by the lack of iron lines (which we show to be an orbital effect) and, secondly, by pure blackbody emission with a temperature of 1.1 keV; this emission can alternatively be fit by a Comptonized accretion disk spectrum in which the scattering electron temperature is close to the seed photon temperature (Koljonen et al. 2010). Thirdly, the state is characterized by a faint power law tail with an index $\Gamma \sim 2$ that spans from 20 keV onward. During the hypersoft state, the hard X-ray flux (15–50 keV band) as measured by the Burst Alert Telescope (BAT) onboard the *Swift* satellite is consistent with zero. At the same time, the soft X-ray flux as measured by the Monitor of All-sky X-ray Image (MAXI) is at its maximum: that is, 1–2 cts cm^{-2} s^{-1} in the 2–20 keV band.

In addition to Cyg X–3, a similar hypersoft state X-ray spectrum has been reported from GRO J1655–40 (Uttley & Klein-Wolt 2015) and Swift J1753.5–0124 (Shaw et al. 2016; albeit here with much lower blackbody/disk temperature). GRO J1655–40 is expected to have a strong magnetically driven accretion disk wind and high inclination (Orosz & Bailyn 1997; Miller et al. 2008; Neilsen & Homan 2012). It has been suggested that the unusually soft spectrum is a consequence of Compton thick and ionized disk wind obscuring the X-ray source in the line of sight (Uttley & Klein-Wolt 2015; Shidatsu et al. 2016; Neilsen et al. 2016). Swift J1753.5–0124 also presented a similar, unusual soft state spectrum, where the accretion disk emission is presumably Compton scattered by a disk atmosphere (Shaw et al. 2016). The observation coincided with a prolonged state of a quenched radio emission (<21 μJy) and zero *Swift*/BAT flux (Rushton et al. 2016). The hypersoft state also bears similarities with ultraluminous supersoft sources that have very soft, thermal, or steep power law ($\Gamma \sim 3$–4) spectra, which produce disk winds due to super-Eddington accretion (Earnshaw & Roberts 2017).

In this paper, we study the hypersoft state of Cyg X–3 preceding the 2016 and 2017 outburst episodes with the Nuclear Spectroscopic Telescope Array (*NuSTAR*), *Swift*, and MAXI in X-rays, and with RATAN-600, the Submillimeter Array (SMA), and the Arcminute Microkelvin Imager (AMI) in the radio together with supporting monitoring observations in γ-rays with the Astrorivelatore Gamma ad Immagini ultra LEggero (AGILE) and the *Fermi* γ-ray Space Telescope. In Sect. 2, we introduce the radio, X-ray, and γ-ray observations and outline their data reduction processes. In Sect. 3, we present the multiwavelength view of the 2016/2017 outbursts and concentrate on the radio, X-ray, and γ-ray properties (spectra and variability) during the hypersoft state. In Sect. 4, based on our observations, we discuss a possible scenario to explain the radio, X-ray, and γ-ray properties by assuming that during the hypersoft state the jet turns off. In Sect. 5, we conclude our findings.

2. Observations and data reduction

We have radio monitoring programs on Cyg X–3 running daily or weekly observations with RATAN-600 and AMI Large Array with higher cadence observing during the outburst episodes. These together with the X-ray monitoring (see below) were used to alert us about the start of the hypersoft state. After triggering, we used target of opportunity and director discretionary's time proposals with the SMA, *Swift*, and *NuSTAR* to study the radio and X-ray properties in more detail. Below, we briefly outline the observations and data reduction processes for each observatory and instrument.

2.1. Radio data

2.1.1. SMA

The SMA, located just below the summit of Maunakea, Hawaii, is an interferometer consisting of eight 6 m diameter antennas configurable to cover baselines ranging from 8 m to 509 m; the SMA has receivers capable of covering frequencies from ~190 to 420 GHz. Observations in 2016 were obtained with a hybrid setup of correlators, covering 8 GHz of bandwidth in each of two sidebands from a single polarization receiver (16 GHz total continuum bandwidth) that has a mean frequency of 225.5 GHz. In 2017, observations were made with the new SMA Wideband Astronomical ROACH2 Machine (SWARM) correlator covering 8 GHz of bandwidth in each of two sidebands from two orthogonally polarized receiving systems (32 GHz total continuum bandwidth), which have a mean frequency of 220–230 GHz. In both years, time spent on source varied between several minutes to several hours. The flux density scale was referenced to the nearby source MWC349A for all observations, providing an absolute flux uncertainty of roughly 5%; however, the relative uncertainty from day to day is much smaller, below 1%.

2.1.2. AMI Large Array

The AMI Large Array, near Cambridge (UK), is the rebuilt and re-engineered 5 km telescope array (Zwart et al. 2008). It has eight 13 m antennas, and operates in the 13 to18 GHz band, with a high-resolution digital correlator. We collected data using the full bandwidth with a center frequency of 15.5 GHz and typically observed the source from ~10 minutes up to a few hours at a time. We used an interleaved calibrator to keep the phases as nearly correct as we can and calibrate the flux density measurements using a calibrator source with a typical variability of 5% in amplitude.

2.1.3. RATAN-600

RATAN-600 is a radio telescope of the Special Astrophysical Observatory of the Russian Academy of Science located in Nizhnij Arkhyz, Russia. The antenna consists of a 576 m circle of 895 reflecting elements that can be used as four independent sectors. Several different feed cabins with secondary mirrors can collect the reflected emission for the primary receivers. The receiver complex consists of several radiometers in the wavelength range spanning from 0.6 GHz to 30 GHz. We used data that were taken with the northern sector at 4.6 GHz, and with the southern sector at 4.8 GHz. The errors on the flux density measurements are ~5 mJy and ~10 mJy for a level of 100 mJy or 3% and 5% at fluxes >1 Jy for the northern and the southern sectors, respectively. In addition, at selected times we took data in the following other bands as well: 2.3, 7.7, 11.2 and 21.7 GHz (see data in Trushkin et al. 2017a,b).

2.2. X-rays

We used X-ray monitoring data from the Gas Slit Camera (GSC; Mihara et al. 2011) of MAXI (Matsuoka et al. 2009) and *Swift*/BAT (Krimm et al. 2013) and obtained the daily and

orbital 2–10 keV and 15–50 keV fluxes from their web interfaces. In addition to the monitoring observations, five pointings were observed with *Swift* (Gehrels et al. 2004) during the outbursts when the source was in the hypersoft state. In addition, one pointing with *NuSTAR* (Harrison et al. 2013) was observed during the decay of a minor flare observed in the middle of the hypersoft state before the major flare ejection in 2017.

2.2.1. *Swift*

The *Swift* X-ray Telescope (XRT; Burrows et al. 2005) windowed timing (WT) mode data were processed using XRTPIPELINE. Sources that are heavily absorbed (including Cyg X–3) show residuals in the WT spectra at low energies (0.4–1.0 keV), when using grades greater than 0. Thus, we extracted only grade 0 spectra. In addition, multipixel events sometimes cross the 10-row binning boundaries of the WT mode and become split during the readout process, which affects the redistribution tail seen in this mode. In order to correct this effect, we used the position-dependent WT redistribution matrices, which correct the spectra at low energies. With these extraction steps, we were able to include the 0.4–1.0 keV data for the X-ray spectra model fitting. The source and background spectra together with the ancillary response are extracted with XRTPRODUCTS. Depending on the source count rate, we extracted the source data from an annulus and background from a circle. For the X-ray modeling we binned the data to $S/N = 10$ in the band 0.5–1.5 keV, $S/N = 20$ in the band 1.5–1.8 keV, $S/N = 30$ in the band 1.8–3.0 keV, $S/N = 40$ in the band 3–6 keV, and $S/N = 30$ in the band 6–10 keV. This gives a roughly equal number of energy bands throughout the spectrum.

2.2.2. *NuSTAR*

We reduced the data from both detectors (FMPA/FMPB) using NUPIPELINE. We used a circular source region with a 60 arcsec radius centered on the location of Cyg X–3, and a circular background region with a 90 arcsec radius that was selected from a sourceless region in the detector image. The pipeline was run with parameters SAAMODE="optimized" and TENTACLE="yes". The former requires the presence of an increase in the CdZnTe detector event count rates simultaneous to the observed shield single rates increase, and the latter allows identification and flagging of time intervals in which the CdZnTe detector events count rates show an increase when the spacecraft is entering the South Atlantic Anomaly (SAA). We extracted a spectrum from both detectors using the whole pointing (~20 ksec), and in addition, divided the pointing to 18 spectra with exposures of ~1 ksec to study the spectral evolution (e.g., orbital modulation). We also extracted light curves from soft (3–10 keV) and hard (20–60 keV) energy bands with 50 second and 100 second time bins, respectively. In addition, we extracted 0.5 s light curve from the full 3–79 keV band to study the fast variability.

For X-ray modeling we binned the data to $S/N = 20$ in the band 3–10 keV, $S/N = 10$ in the band 10–20 keV, and $S/N = 5$ in the band 20–79 keV. This gives a roughly equal number of energy bands throughout the spectrum.

For the timing analysis, we calculated the cospectra from the continuous data segments of the 0.5 s light curves of both detectors. The cospectrum is the real part of the complex cross spectrum that is the Fourier transform of a time series (in this case the light curve from FMPA) multiplied with the complex conjugate of the Fourier transform of another time series (the light curve from FMPB). The cospectrum is used to mitigate instrumental effects, especially dead time that is present in the *NuSTAR* light curves (Bachetti et al. 2015), and can be used as a proxy for the (white-noise-subtracted) power density spectrum (PDS). We calculated the cospectra using MaLTPyNT (Bachetti 2015), which are then used to make an average cospectrum.

Table 1. X-ray observations

Swift pointing	Start date MJD	Exp. [ksec]	Start phase
00031922032	57626.33859	0.98	0.52
00031922033	57629.65261	0.97	0.11
00059162001	57801.61197	1.55	0.23
00059163001	57801.67723	1.55	0.55
00059164001	57801.74321	1.55	0.88
NuSTAR pointing	Start date MJD	Exp. [ksec]	Elapsed [ksec]
90202051002	57814.23476	14.3	43.7

2.3. γ-rays

We used γ-ray monitoring data from the γ-Ray Imaging Detector (Barbiellini et al. 2002; Prest et al. 2003) onboard AGILE (Tavani et al. 2009a). The data were collected during both outburst episodes including the hypersoft states. We registered only those events that present TS values over 6. The data reduction and analysis methods are described in Piano et al. (2012).

In addition to AGILE data, we used reported *Fermi* Large Area Telescope (LAT) detections (Cheung & Loh 2016) for the 2016 outburst episode, and the data from *Fermi*-LAT monitored source list[1] for the 2017 outburst event.

3. Results

3.1. Multiwavelength overview

During the multiwavelength campaign of Cyg X–3 in 2016 and 2017, the source presented similar behavior for both outburst episodes (Fig. 1). The hypersoft state preceded the major outburst for a length of ~20 days and ~45 days for 2016 and 2017, respectively, interspersed by moderate radio (radio flux densities reaching 1 Jy) and hard X-ray flaring (correlated with the radio). On average, the 2017 outburst presented slightly higher radio flux densities throughout the outburst episode including the hypersoft state, in which the (frequency-independent) radio flux density varied between 10–100 mJy during zero flux from *Swift*/BAT, while in 2016 the radio flux level was lower at 1–20 mJy.

Several ATels reported γ-ray detections during the 2016/2017 outburst episodes. In 2016, a γ-ray flare was observed at the onset of the minor radio flare (Piano et al. 2016; Cheung & Loh 2016). In 2017, three flares were reported: one in transit into the hypersoft state, one during a minor radio flare, and one at the onset of the major radio flare (Loh & Corbel 2017a,b; Piano et al. 2017a,b).

3.2. Radio properties

Intraday radio light curves during the hypersoft state show strong radio modulation with ~0.1 day flares in 15 GHz and

[1] https://fermi.gsfc.nasa.gov/ssc/data/access/lat/msl_lc/

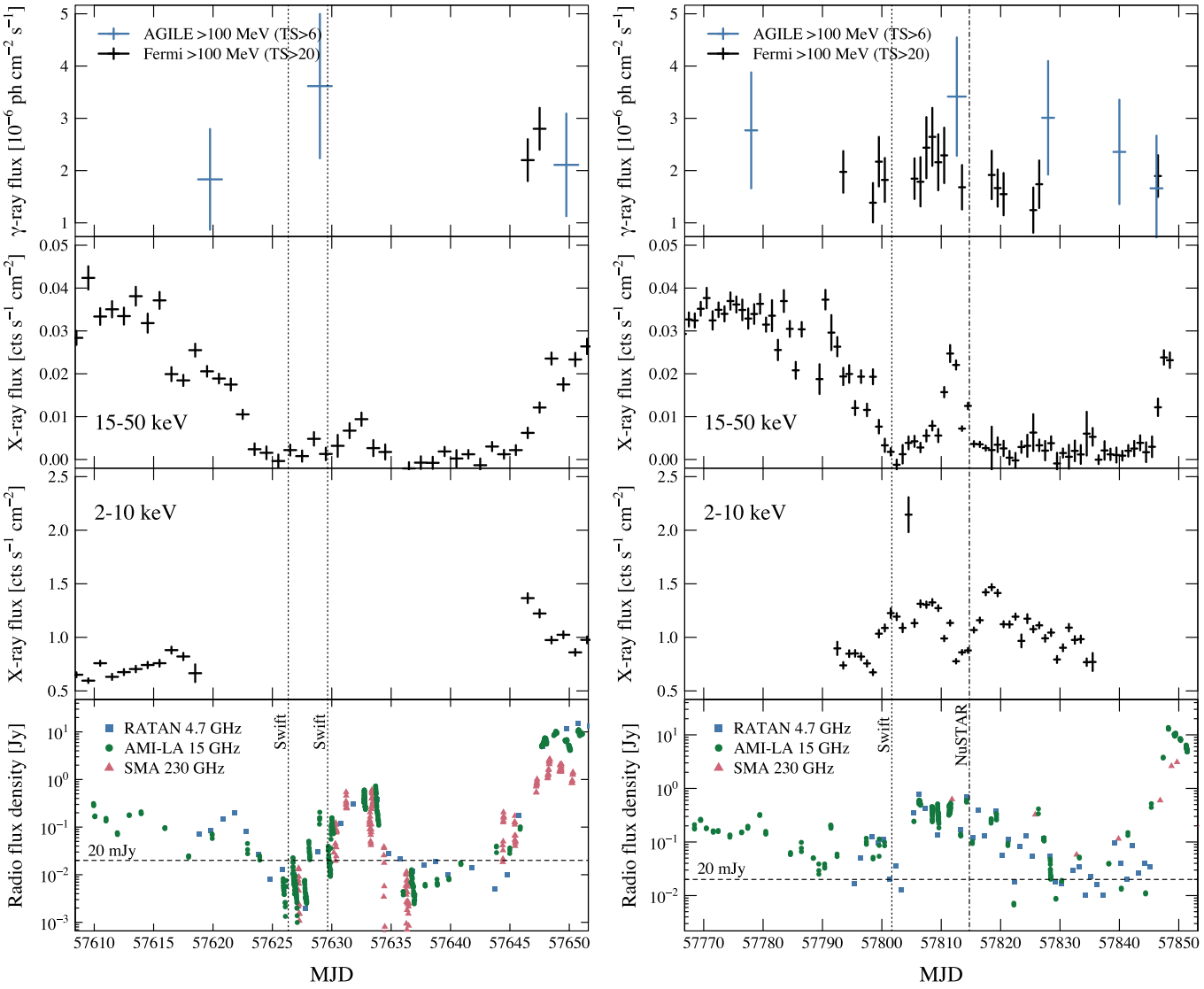

Fig. 1. *Left:* γ-ray (AGILE and *Fermi*), X-ray (*Swift*/BAT and MAXI), and radio (RATAN, AMI-LA, and SMA) monitoring of the 2016 outburst episode. *Right:* The same monitoring campaign for the 2017 outburst. Hypersoft state occurs when the *Swift*/BAT 15–50 keV count rate is approximately 0 cts s^{-1} cm^{-2}, and radio flux is below 20 mJy. Usually, a prolonged (~10–30 days) hypersoft state occurs before outbursts, which can also exhibit brief (few days) flares in the radio and hard X-rays, as happened in both 2016 and 2017 outbursts. γ-ray emission is usually attributed to changes to/from the hypersoft state (during the onset, and/or during the hard X-ray/radio flare, and/or during the onset of the outburst). Dotted and dot-dashed lines denote *Swift* and *NuSTAR* pointings, respectively.

fast (~20–50 minutes) flickering in 230 GHz (Figs. 2, 3). These variability timescales correspond to emission regions of $3{\times}10^{14}$ cm and $3{-}9\times10^{13}$ cm, respectively, and both lie well beyond the orbital separation that for 4.8 hour orbital period and 10–20 $M_\odot$ total mass of the binary is $2{-}3\times10^{11}$ cm.

Assuming that the jet radio emission is attenuated by free-free absorption in the WR stellar wind (Fender et al. 1995; Waltman et al. 1996), the radio photosphere R for a given frequency ν can be approximated as (Wright & Barlow 1975; Waltman et al. 1996)

$$R_{\tau\sim1} = 1.75\times10^{28}\gamma^{1/3}g_{ff}^{1/3}Z^{2/3}T^{-1/2}\left(\frac{\dot{M}}{\mu v_\infty \nu}\right)^{2/3}\ \mathrm{cm}, \quad (1)$$

where the free-free Gaunt factor, g_{ff}, is derived from the relation (Leitherer & Robert 1991):

$$g_{ff} = 9.77\times\left[1.0 + 0.13\log\left(\frac{T^{3/2}}{\nu Z}\right)\right]. \quad (2)$$

Using the following parameters for the stellar wind (Koljonen & Maccarone 2017), the mass-loss rate of $\dot{M} = 10^{-5}\,M_\odot$/yr, temperature of $T = 45000$ K, terminal velocity of the stellar wind of $v_\infty = 1000$ km/s, rms ionic charge of $Z = 1$, mean number of free electrons per nucleon of $\gamma = 1$, and mean atomic weight per nucleon of $\mu = 3.6$, we get 5×10^{13} cm and 7×10^{12} cm for the 15 GHz and 230 GHz photosphere radii. Thus, these values are consistent with the variability timescales.

We calculated the fractional variability amplitude (Vaughan et al. 2003, and references therein; also known as the coefficient of variation) from the intraday 15 GHz and 230 GHz radio fluxes (Fig. 4). We disregarded the observations that presented less than 10 subsequent radio measurements. The amplitude of the radio variability is at its maximum during the hypersoft state and the radio flux exhibits variations that exceed the average flux. During radio flares the amplitude decreases more strongly for the outburst than during moderate radio flaring. If the radio variability is connected to the light-crossing time of the emission region,

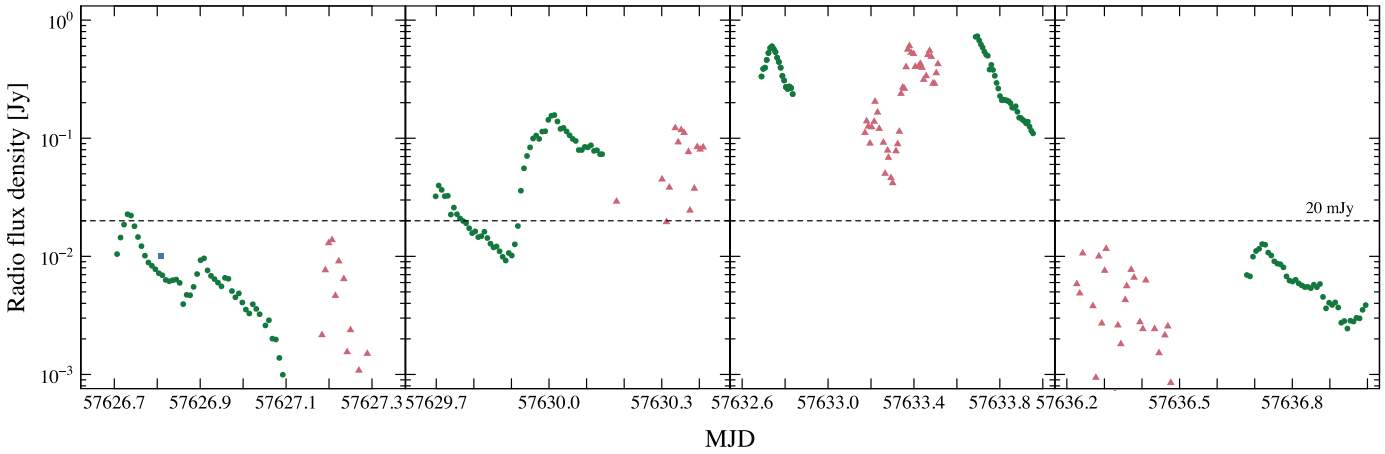

Fig. 2. Intraday radio light curves (green: 15 GHz, red: 230 GHz) from the 2016 hypersoft state (*first and last panels*) and minor radio flare (*middle panels*). The colors are same as in Fig. 1. The 230 GHz light curve seems to present higher variability (see Fig. 3 and 4). The 15 GHz light curve presents some well-defined flares that last ~0.1 days, indicating a size scale of 3×10^{14} cm (well beyond the orbital scale).

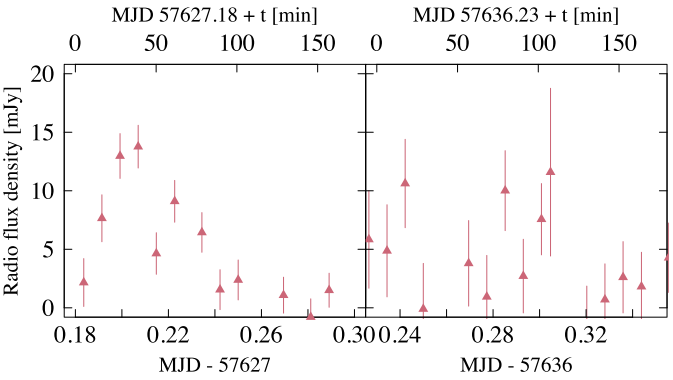

Fig. 3. Light curve of 230 GHz during hypersoft state presenting rapid flickering with ~20–50-minute timescale, indicating a size scale of $3–9 \times 10^{13}$ cm (well beyond the orbital scale).

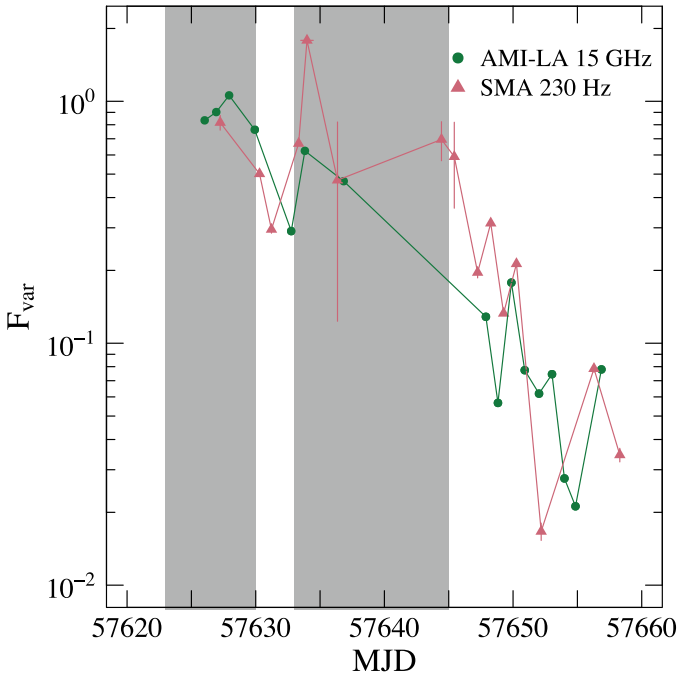

Fig. 4. Fractional variability amplitude (coefficient of variation) of the radio light curves (green: 15 GHz, red: 230 GHz). The evolution in the 15 GHz and 230 GHz is similar. Also, during the hypersoft state (around MJD 57625 and MJD 57635, colored areas) the fractional variability amplitude is at maximum and presenting variations exceeding the mean, while during the flares it is markedly lower.

this indicates that the hypersoft state presents more compact emission regions.

During the hypersoft state the simultaneously measured radio spectrum from 4.6 GHz to 11.2 GHz is mostly inverted, that is, optically thick ($F_\nu \propto \nu^\alpha$; $\alpha \sim 1$), while during minor radio flaring it is flatter ($\alpha \sim 0$; Fig. 5) or optically thin. On the other hand, when we have quasi-simultaneous observations (within 0.5 days) in 15 GHz and 230 GHz bands, the spectrum is approximately flat during both states. However, during the hypersoft state, even slight changes in the radio fluxes can result in a big change in the spectral index and depend on strict simultaneity (which we do not have for the 15 GHz and 230 GHz bands) as they vary quite rapidly (see above). Overall, we can state that during the hypersoft state the low radio frequencies are absorbed below ~10 GHz, and during minor radio flaring the absorption frequency moves progressively below 5 GHz, while the radio spectra above 10 GHz remains approximately flat in both states.

The spectral curvature is evident from one example of a quasi-simultaneous (0.6-day difference between RATAN-600 and SMA observations) radio spectrum shown in Fig. 6 that was taken during the beginning of minor radio flaring in the 2016 outburst episode (MJD 57631.2–57631.8). The spectrum can be adequately fitted by a model of the form (van der Laan 1966; Gregory & Seaquist 1974)

$$S_\nu = \frac{S_0}{1-\exp(-1)}\left(\frac{\nu}{\nu_0}\right)^{\alpha_{thick}}\left(1-\exp\left[-\left(\frac{\nu}{\nu_0}\right)^{\alpha_{thin}-\alpha_{thick}}\right]\right)\times f(\nu), \quad (3)$$

where S_0 and ν_0 are the flux density and the frequency at which $\tau = 1$, α_{thin} and α_{thick} correspond to an optically thin and thick spectral index below and above ν_0, respectively, and $f(\nu)$ depends on the absorption mechanism. See more discussion in Sect. 4.1.

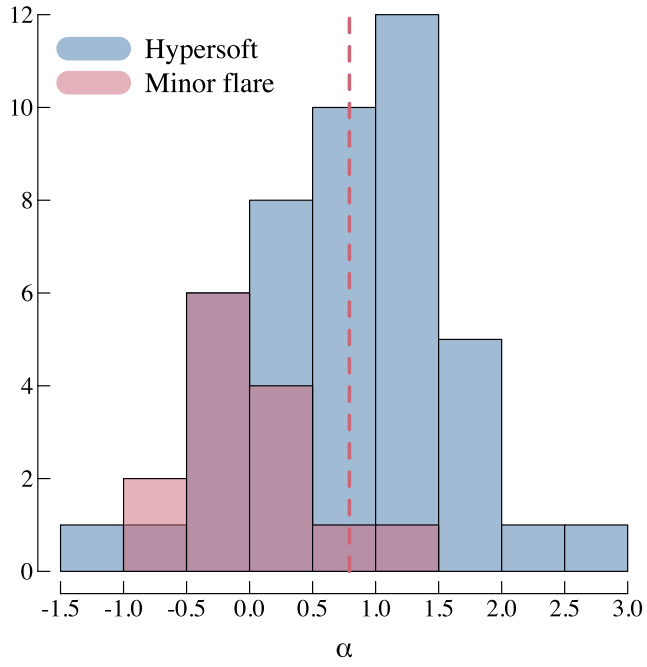

Fig. 5. Histogram of the radio spectral index using RATAN-600 data from 4.6 GHz to 11.2 GHz during the hypersoft state (blue) and the minor radio flaring state (red). The radio spectrum during the hypersoft state is mostly inverted, optically thick, while in the minor flaring state it is flatter or optically thin. The spectral index during the radio spectrum shown in Fig. 6 is indicated as a dotted line.

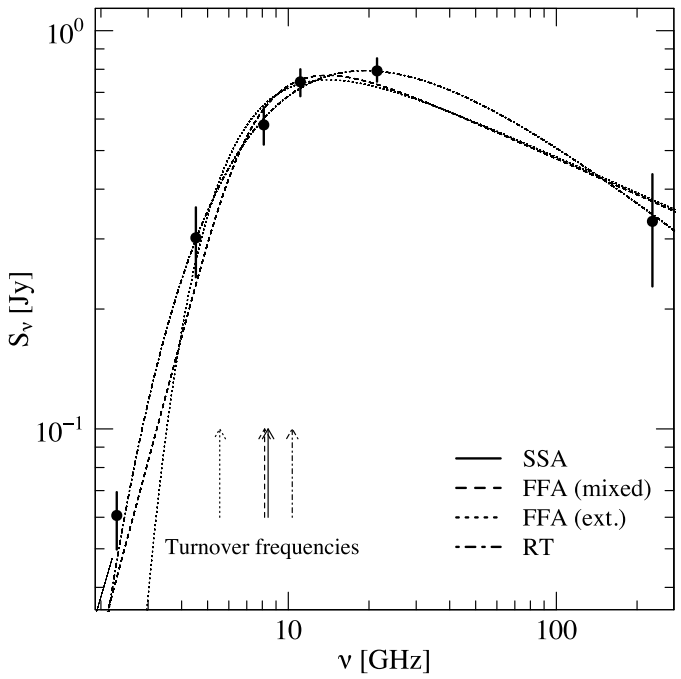

Fig. 6. Quasi-simultaneous radio spectrum from RATAN-600 (2–22 GHz; the data in all bands was taken simultaneously on MJD 57631.8) and SMA (230 GHz; the data was taken on MJD 57631.2). The data point for the SMA is an average over the 1.5 hour exposure and the error bars indicate the standard deviation of the measurements during the exposure. The spectrum is fitted with several models (SSA: synchroton self-absorption, FFA: free-free absorption, RT: Razin-Tsytovitch effect). See text for more details.

3.3. X-ray properties

In Fig. 1 we see that the *Swift*/BAT daily light curve follows roughly the evolution of the radio emission in the sense that during the hypersoft state the hard X-ray flux and radio flux density reach their minima and they rise and decay in unison (on a long-term basis from days to weeks) during flaring episodes. This correlation was established already in McCollough et al. (1999). In contrast, the soft X-ray flux is at its maximum during the hypersoft state (MAXI 2–10 keV mean flux of 1 cts s^{-1} cm^{-2}, and flares up to 2 cts s^{-1} cm^{-2}, as compared to 0.4 cts s^{-1} cm^{-2} in the low/hard X-ray state). The soft X-rays are also roughly anti-correlated with the hard X-rays during the hypersoft state, but a robust measure of anticorrelation is difficult to attain because of the negligible *Swift*/BAT flux.

3.3.1. X-ray spectrum

As has been found previously, the X-ray spectrum during the hypersoft state is soft; the dominating component being blackbody-like in addition to a weak power law tail (Koljonen et al. 2010; Smale et al. 1993; Beckmann et al. 2007; Szostek & Zdziarski 2005). In these previous works, the soft component was successfully fitted with a one-temperature blackbody, multicolor blackbody, or heavily thermalized Comptonization model (resembling a blackbody), and the hard component was fitted either as Compton upscattered emission from the soft seed photons or a power law model.

Thus, we started fitting the orbital *NuSTAR* spectra (∼1 ksec; see Fig. 7 and 8) from both detectors simultaneously with a model consisting of a blackbody component (BBODY) convolved with a Comptonization model (SIMPL; Steiner et al. 2009) and attenuated by interstellar absorption (PHABS). This would indicate a scenario in which the soft photons are heavily thermalized to one-temperature plasma, for example, by the interaction of the stellar wind with the accretion disk (Zdziarski et al. 2010). In addition, we add an iron line complex (see Paerels et al. 2000) and absorption edges of neutral and highly ionized iron. The iron line complex was fitted with a single Gaussian line, but likely consisted of neutral, and several highly ionized, iron emission lines. We also considered a model in which the hard X-ray tail was fitted with a power law in case it is not connected to the blackbody component, for example in a situation where the hard X-rays are upscattered infrared photons from the jet or optically thin synchrotron emission from the jet. Both models resulted in acceptable fits ($\chi^2_{\rm red}$ = 0.9–1.4), however the power law model resulted in a higher absorption column (about twice), as the soft photons are not removed by the Compton scattering. The parameters of the orbital fits with the Comptonization component are plotted in Fig. 9.

For both power law and Comptonization models, the blackbody temperature stayed constant at $kT_{\rm bb}$ = 1.35 ± 0.05 keV for the whole *NuSTAR* observation. The blackbody luminosity is orbitally modulated and peaks at $L_{\rm bb} = 10^{38}$ erg/s (for a distance of 7.4 kpc) during orbital phase 0.5. Alternatively, we fitted the thermal component with a multicolor disk blackbody model (EZDISKBB) with equally good fit quality as the blackbody model, but with increased absorption (two to three times the blackbody model) and a higher temperature ($kT_{\rm bb}$ = 1.7 keV).

The column density of the absorption component is orbitally modulated exhibiting highest values, $N_{\rm H} \sim 4\times10^{22}$ cm^{-2}, during orbital phase 0.1–0.3 (likely representing local absorption) and

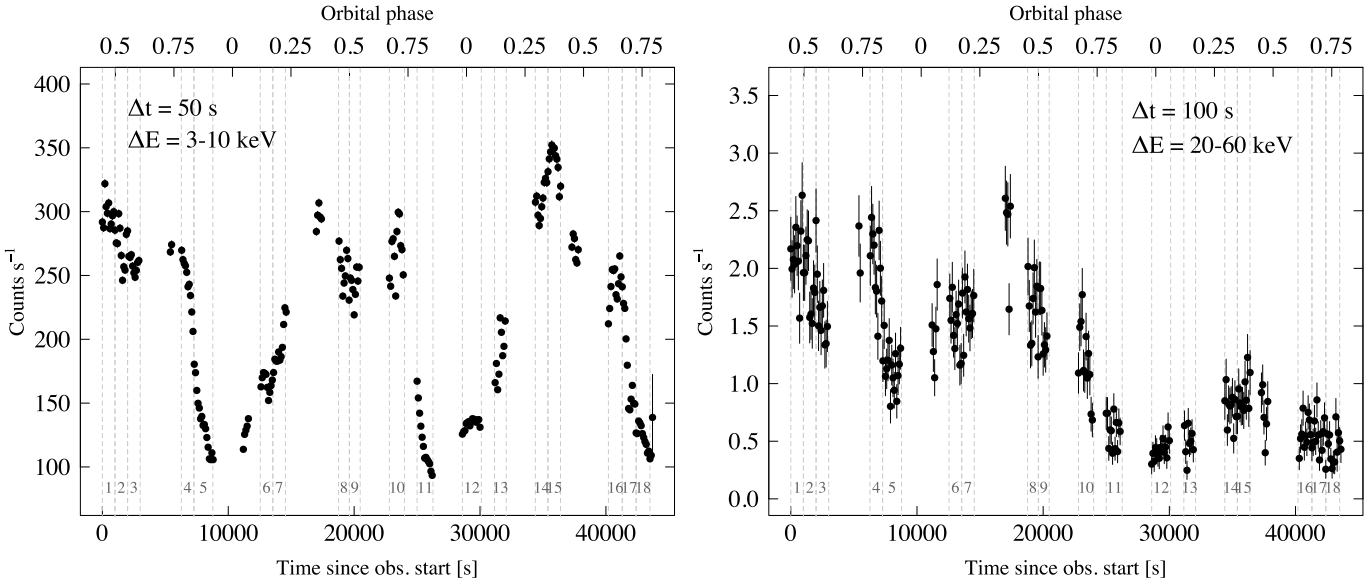

Fig. 7. *Left: NuSTAR* count rate in band 3–10 keV during the whole pointing spanning ~2.5 orbits. The orbital phase is labeled on top of the panels. This spectral band consists almost solely of the blackbody emission. *Right: NuSTAR* count rate in the band 20–60 keV. This spectral band consists of only the power law emission. The dashed lines demarcate the ~1 ksec *NuSTAR* spectra that are shown in Fig. 8.

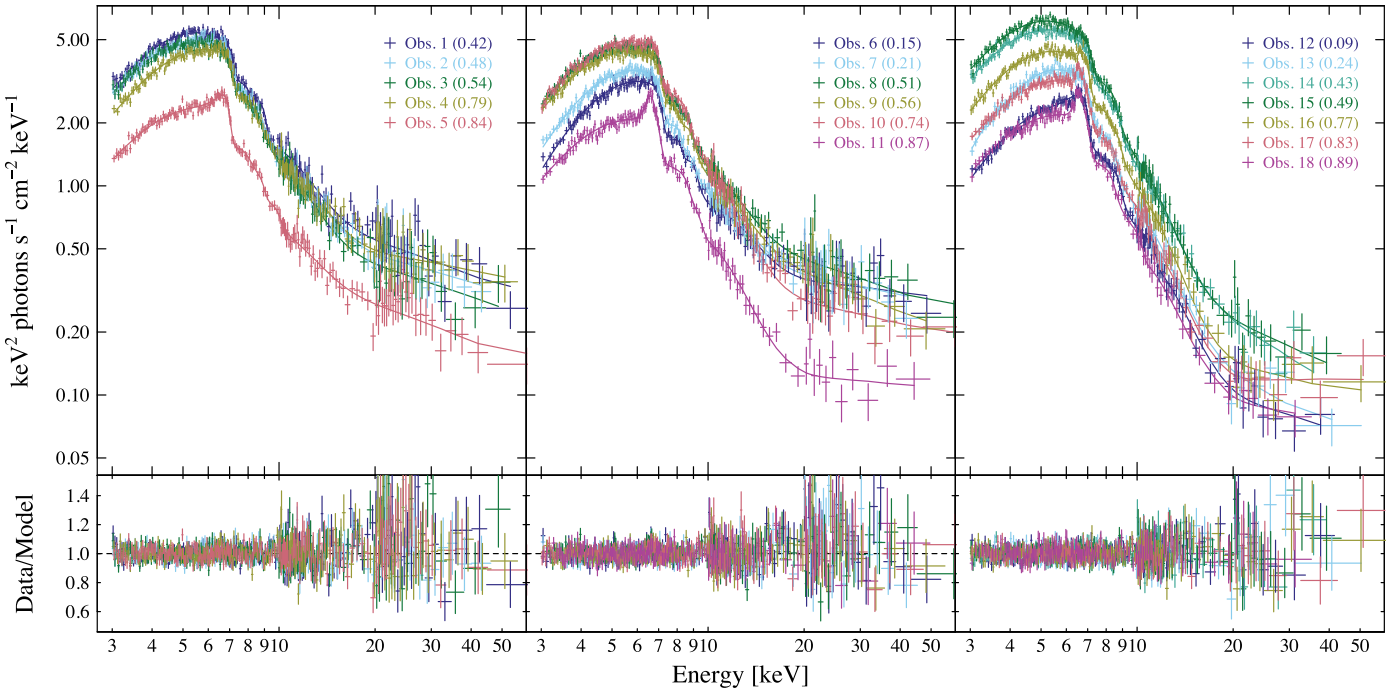

Fig. 8. *NuSTAR* spectra with ~1 ksec exposure through the whole pointing spanning ~2.5 orbits. Orbital phase is indicated in parenthesis (*left panel*: first half orbit, *middle panel*: second orbit, *right panel*: third orbit). The spectra are fitted with a model consisting of absorbed blackbody, Comptonization, and Gaussian components multiplied by three absorption edges from neutral and ionized iron. The model residuals are shown in the bottom panels. The plotted spectra are from FMPA for clarity, but the models are fitted to both detectors simultaneously.

otherwise $N_{\rm H}$ = 1.5–2.0 × 10^{22} cm^{-2}, which is consistent with the value of the interstellar 21 cm absorption component to the direction of Cyg X–3: $N_{\rm H}$ ~ 1.6 × 10^{22} cm^{-2} (Dickey & Lockman 1990). Thus, in order to allow models with a multicolor disk blackbody and/or a power law component, it is necessary to explain the increased, constant absorption in addition to the interstellar component.

When using the power law model, the photon power law index stayed approximately constant at Γ = 2.5 ± 0.3. In the case of the Comptonization model, the fraction of seed photons scattering from the electron population is $f_{\rm Comp}$ ~ 0.1 in the first two orbits, but drops to half of that during the end of the second orbit (during 3–4 ksec time frame) reflecting the drop in the Comptonized flux. This can be also seen as a drop in the hard X-ray flux in Fig. 7. It is notable that at the same time the radio emission (at 4.6 GHz and 15 GHz) drops from ~600 mJy to ~100 mJy (Fig. 1).

The absorption edges are found to be at energies $E_{\rm Fe/N}$ = 7.1−7.2 keV (neutral iron), $E_{\rm Fe/He}$ = 8.2−8.5 keV, and $E_{\rm Fe/H}$ = 9−10.5 keV (highly ionized iron; helium- and

hydrogen-like, respectively). The helium-like edge can be fit better with a smeared edge model (SMEDGE) with its width fixed to τ = 0.5 keV, most likely because of the multiple components from the edge profile (Kallman et al. 2004). There are hints that the optical depth of the absorption edges is reduced at phase 0.5, especially in the case of the third orbit.

The Gaussian line is evident in the data only at orbital phase ~0.8–0.1 (Fig. 8). This is consistent with what was found in Vilhu et al. (2009), where the iron line flux maximum was attributed close to phase 0.0. These authors speculated that the orbital phasing of the line photons is due to electron scattering and broad line absorption in the vicinity of the compact object. The centroid energies of the Gaussian line are found in the range of $E_{\rm Fe}$ = 6.6–6.7 keV, thus marking the influence of the highly ionized iron in the iron complex, which is consistent with the detection of the highly ionized iron edges. The widths of the Gaussian line range between $\sigma_{\rm Fe}$ = 0.2–0.4 keV and the line fluxes range between $F_{\rm Fe}$ = 0.010–0.016 photons s^{-1} cm^{-2}.

The *Swift* spectra (see Fig. 10) can be adequately ($\chi^2_{\rm red}$ = 1.2–1.7) fitted with an absorbed blackbody model modified by a template of emission/absorption lines and radiative recombination continua (Savolainen 2012; Koljonen et al. 2013, McCollough et al., in prep.). The best fit parameters are plotted in Fig. 11. All phases have $N_{\rm H} \sim 4 \times 10^{22}$ cm^{-2} ; however, if $N_{\rm H}$ is frozen to 4×10^{22} cm^{-2} in fitting the *NuSTAR* spectra, it does not result in an acceptable fit outside phase range 0.1–0.3. There is slightly higher absorption ($N_{\rm H} \sim 4.5 \times 10^{22}$ cm^{-2}) during phase 0.2–0.3 similar to (but not in proportion to) the *NuSTAR* spectra. Thus, it is possible that the *Swift* spectra occurring in the hypersoft state present more absorption than during the decay of the minor radio flare that coincided with the *NuSTAR* pointing. The emission/absorption lines and radiative recombination continua arise from photoionization of the stellar wind by the intense X-ray radiation (Paerels et al. 2000; Szostek & Zdziarski 2008). However, a Gaussian line component to model the iron line complex is only statistically needed for the last pointing in 2017 with a centroid energy $E_{\rm Fe}$ = 6.8 keV, width $\sigma_{\rm Fe}$ = 0.2 keV, and a flux $F_{\rm Fe}$ = 0.02 photons s^{-1} cm^{-2}. Similar to the *NuSTAR* spectra, the temperature of the blackbody model is around $kT_{\rm bb}$ = 1.3 keV, except for the last pointing where it dropped to $kT_{\rm bb}$ = 1.2 keV. The effect is clearly visible in the spectrum (Fig. 10) as a reduced flux over 4 keV and cannot be attributed to a change in the absorption profile. As the 2017 *Swift* pointings occurred at the same date in a subsequent fashion, we can state that the X-ray emitting surface cooled from 1.3 keV to 1.2 keV during a time frame of 1.3–1.6 hours. Similar to the *NuSTAR* results, the blackbody flux is orbitally modulated with a slightly higher maximum of $L_{\rm bb} = 1.2 \times 10^{38}$ erg/s as compared to the *NuSTAR* spectra during phase 0.5. It is interesting to note that the blackbody flux in the last pointing in 2017 does not present unusually low flux with respect to the orbital variation, thus the cooling of the blackbody temperature could imply a rapid change in the blackbody radius.

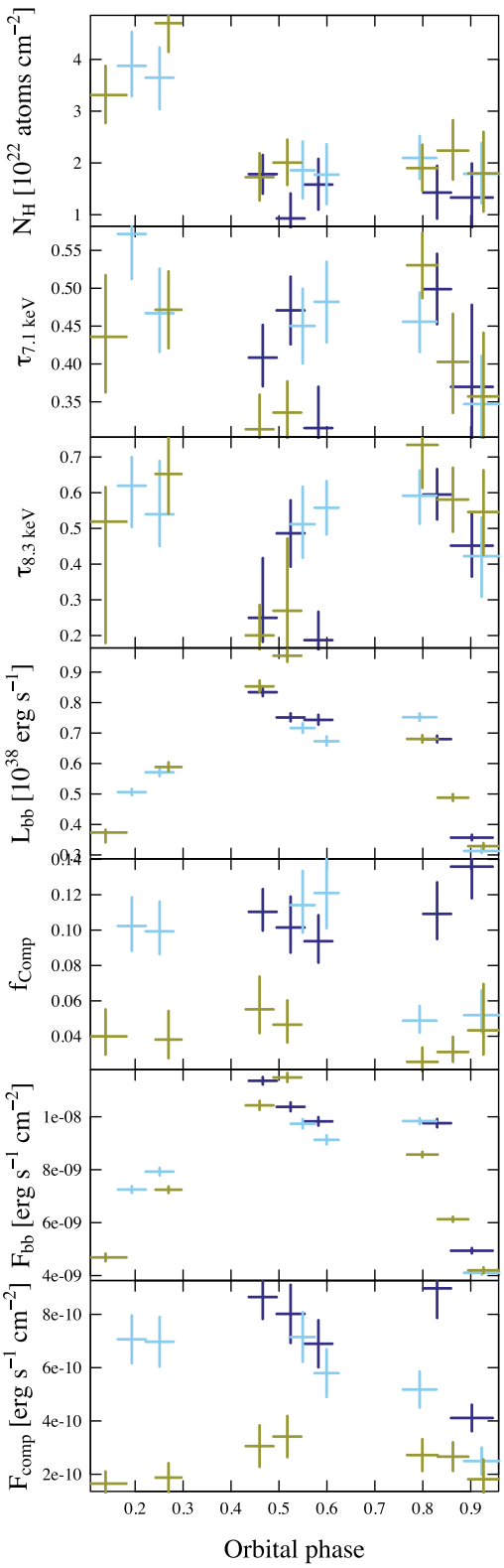

Fig. 9. X-ray model parameter evolution over the orbital phase using the *NuSTAR* data. The different colors indicate different orbits during the ~20 ksec exposure: blue corresponds to the first, light blue to the second, and green to the third orbit. *From top to bottom*: the hydrogen column density, optical depths of the neutral and helium-like iron, bolometric blackbody luminosity assuming a distance of 7.4 kpc, fraction of Compton upscattered seed photons, and unabsorbed blackbody and Comptonized fluxes calculated from the *NuSTAR* energy band 3–79 keV are shown.

3.3.2. X-ray light curve

We construct the averaged cospectrum (the real part of the cross spectrum, see Sect. 2.2.2) from the *NuSTAR* 0.5 s time resolution light curves (Fig. 12). The cospectrum technique is used to mitigate the instrumental dead noise in estimating the periodogram of the source. As has been found out previously in Axelsson et al. (2009); Koljonen et al. (2011), the PDS of Cyg X–3 can be described as a power law with an index close to β = −2

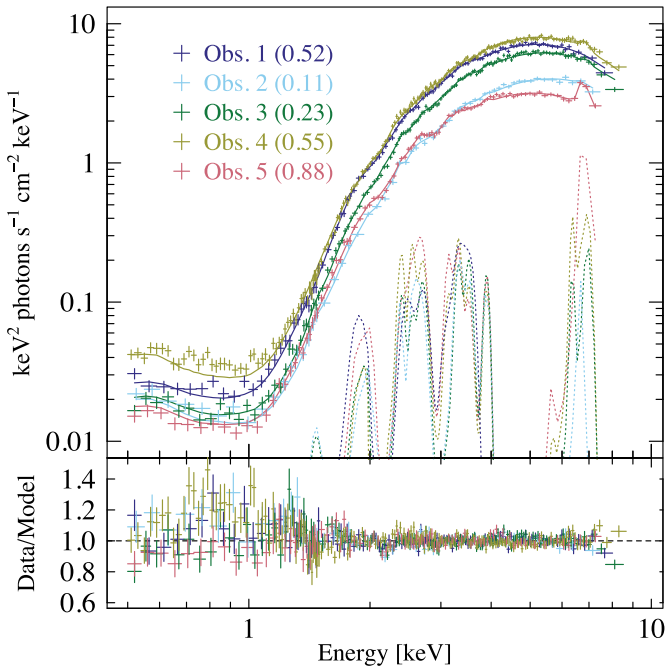

Fig. 10. *Swift*/XRT spectra with ∼1 ksec exposure from 2016 (obs. 1–2) and 2017 outbursts (obs. 3–5). The orbital phases are indicated in parenthesis. The spectra were fitted with a model consisting of an absorbed blackbody modified by a template of absorption/emission lines and radiative recombination continua (dotted lines). The model residuals are in the *bottom panel*.

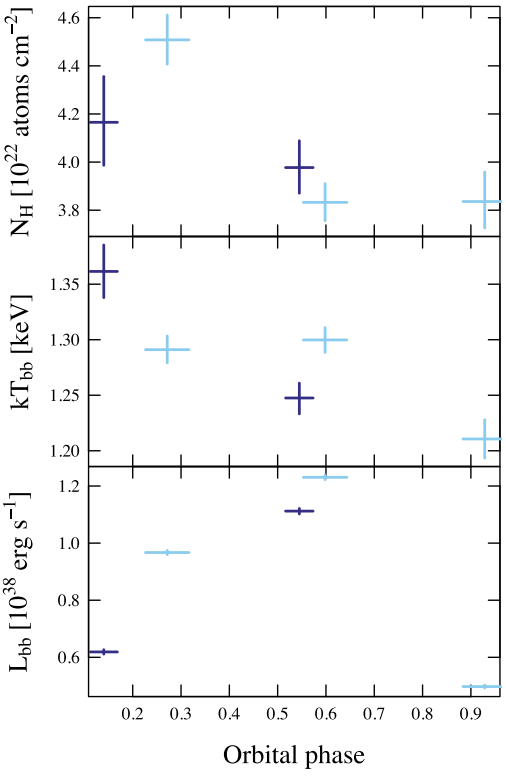

Fig. 11. X-ray model parameter evolution over the orbital phase using the *Swift* data. The various colors indicate the different times: blue corresponds to the observations taken in 2016 and light blue in 2017. *From top to bottom*: hydrogen column density, temperature of the blackbody, and bolometric blackbody luminosity assuming a distance of 7.4 kpc are shown.

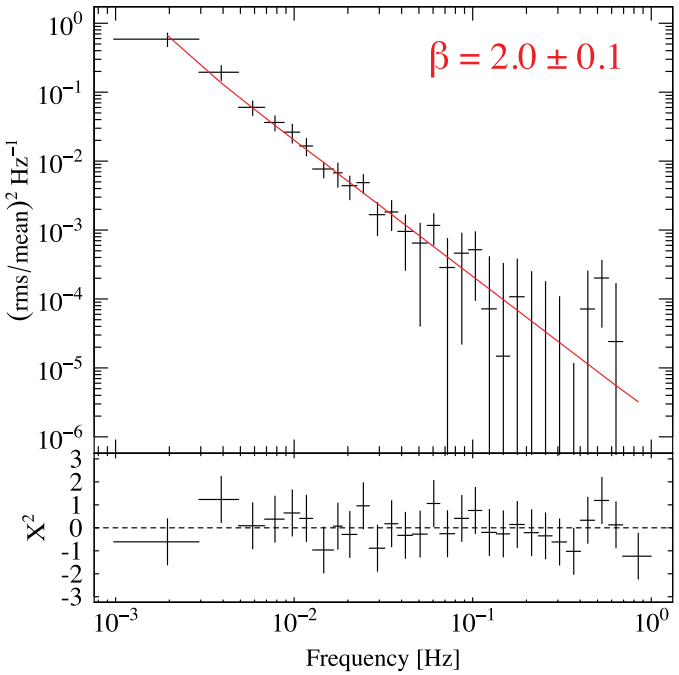

Fig. 12. *NuSTAR* averaged cospectrum fitted with a power law model.

with hardly any other structure. In addition, there seems to be no power above 1 Hz. Thus, we fitted the averaged cospectrum with a power law model. Similar to previous results, we find that the power law index is $\beta = -2.0 \pm 0.1$.

4. Discussion

To summarize the above observational and modeling results of the hypersoft state we found the following:

1) The X-ray spectrum can be successfully modeled phenomenologically by using a simple model consisting of a single-temperature blackbody and a power law component. The power law component could arise from the Compton upscattering of the 1.3 keV blackbody photons from a population of high-energy electrons that are moving or changing the subtended angle as viewed from the seed photon population in ksec timescales. Alternatively, this could arise from the optically thin jet emission spanning the X-ray band or Compton upscattered infrared photons from the jet. Both models resulted in acceptable fits; the only difference in the amount of absorption was close to the interstellar value in the former and twice the interstellar value in the latter. The exception to this was in orbital phases 0.0–0.3, where local absorption is present in both cases. The single-temperature blackbody model can be also exchanged for a multicolor blackbody component, but again with the expense of introducing a higher absorption column (a factor of 2–3) and a higher blackbody temperature.

2) There are strong absorption edges present in the X-ray spectra indicating screens of neutral and ionized iron in the line of sight, and ionized iron line that is visible in the X-ray spectra only at orbital phases 0.8–0.0, most likely occurring in a photoionized region close to the compact object.

3) The X-ray cospectrum (a proxy for PDS) is similar to what is observed in the PDS of every other spectral state: power law with an index of $\beta = -2.0$.

4) The radio spectrum is approximately flat (or slightly inverted) from ∼10 GHz to 230 GHz (also during the ∼ 1 Jy radio

flare) and presents the lowest fluxes in the source evolution down to 1 mJy level, where the radio variability is at its maximum. During the hypersoft state and at the beginning of a minor radio flare, the radio fluxes below 10 GHz are absorbed with a relatively high index indicative of free-free absorption, synchrotron self-absorption, or a Razin-Tsytovitch effect. The radio emission was also found to be coupled to the hard X-ray emission in orbital timescales.

5) Significant γ-ray emission usually occurs during the hypersoft state. In particular, at times corresponding to the onset of the hypersoft state, the onset or during the minor radio flare, and during the onset of the major radio flare. All of these were observed in the 2016 and 2017 data sets.

4.1. Origin of the radio emission

The radio spectrum was previously speculated to arise as a synchrotron emission from expanding plasmons (e.g., Marti et al. 1992; Fender et al. 1997) or shocks in the jet (Lindfors et al. 2007; Miller-Jones et al. 2009). Following Gregory & Seaquist (1974) and Miller-Jones et al. (2004), this emission is thought to be absorbed either by synchrotron self-absorption, free-free absorption by thermal plasma uniformly mixed with or surrounding the synchrotron emitting particles, or a suppression of synchrotron radiation by a dispersive medium in a so-called Razin-Tsytovitch effect (Hornby & Williams 1966; Simon 1969). Of course, a mixture of these processes could also take place, but in the following, we consider them separately. The low-frequency cut-off could also arise from induced Compton scattering (Sincell & Krolik 1994) or a low-energy cut-off in the electron spectrum. However, in the latter case, the slope below the turnover would be $\alpha_{thick} \sim 0.3$, which is too shallow to account for the observations.

In the above, it was speculated that the radio emission during the hypersoft state is likely similar to what was observed during the beginning of the minor radio flare. We have fitted the minor flare radio spectrum (Fig. 6) with a nonthermal model absorbed by the above-mentioned absorption processes according to Eq. (3). For the synchrotron self-absorption ($f(\nu) = 1$), setting $\alpha_{thick} = 2.5$ and $\alpha_{thin} = -0.3$ produced an acceptable fit to the spectrum. Previously, the synchrotron self-absorption has been deemed as sufficient to explain fully the absorption of the radio flux densities in the shock-in-jet model during major and minor radio flares (Miller-Jones et al. 2009). The synchrotron self-absorption turnover frequency is given approximately as (e.g., Kellermann & Pauliny-Toth 1981),

$$\nu_0 \sim f(\gamma) B^{1/5} S_0^{2/5} \theta^{-4/5} \,\mathrm{GHz}, \quad (4)$$

in the case of uniform source and power law distribution of particles with an index γ. The function f(γ) does not depend strongly on γ, and it is f(γ) $\sim$ 8 if $\gamma = 2$. With the flux density of $S_0 = 0.7$ Jy during the peak of the minor radio flare, and a VLBI source angular size $\theta \sim 1$ mas (Egron et al. 2017, also corresponds to the radio photosphere size at 15 GHz from Eq. (1)), the magnetic field strength should be 6–100 G. If assuming that the same spectral shape applies to the hypersoft state where $S_0 \sim 0.01$ Jy, the magnetic field strength should be much larger ($>3 \times 10^4$ G). These values are much larger than estimated previously (~0.1 G; Gregory & Seaquist 1974; Fender et al. 1997; Miller-Jones et al. 2004). However, as the radio images of Cyg X–3 are scatter-broadened, the true source size is difficult to determine, and therefore the magnetic field strength could be lower.

Synchrotron self-absorption becomes important for sources with brightness temperatures $T_b > m_e c^2/3k \sim 2 \times 10^9$ K. The brightness temperature of Cyg X–3 can be approximated from the duration of a flare and its flux change (Ogley et al. 2001):

$$T_b \geq 9.66 \times 10^{10} \frac{\Delta S\, D^2}{\nu^2 \Delta t^2} \,\mathrm{K}, \quad (5)$$

where S is in units of mJy, D in kpc, ν in GHz and t in minutes. During hypersoft state (see Fig. 2) the flare duration $\Delta t \sim 0.1$ day (140 minutes), flux change of $\Delta S = 10$ mJy at $\nu = 15$ GHz and a distance of $D = 7.4$ kpc implies brightness temperature of $T_b \geq 1 \times 10^7$ K (at the minor flare peak it increases to $T_b \geq 3 \times 10^8$ K). Thus, this value is too low for the synchrotron self-absorption to take place unless the source size is much smaller than implied by the flare duration. Therefore, we cannot rule out the synchrotron self-absorption as a possible mechanism for the observed absorption, but we deem it unlikely, as such a high synchrotron self-absorption turnover frequency have not been observed from any other flat radio spectrum XRB, and if observed they have been found to lie below 1 GHz. The low brightness temperature would also exclude induced Compton scattering as causing the turnover.

The mixed free-free absorption has been proposed previously to best represent the absorbed radio spectrum (Gregory & Seaquist 1974) and to explain the decreasing opacities in a series of radio flares (Fender et al. 1997). Here, the thermal plasma surrounding the compact object is thought to be entrained in the jet during the launching of the jet after the quenched period. For the mixed free-free absorption ($f(\nu) = 1$), setting $\alpha_{thick} = 2.1$ and $\alpha_{thin} = -0.3$ in Eq.(3) produced also an acceptable fit to the spectrum (Fig. 6).

The external free-free absorption has been discussed in Fender et al. (1995); Waltman et al. (1996) to be the cause of the absorption as an absorbing screen of thermal plasma likely from the WR wind. The radio spectrum can be fitted with the external free-free absorption by setting $\alpha_{thick} = \alpha_{thin} = -0.3$ and $f(\nu) = \exp[-(\nu/\nu_0)^{-2.1}]/\exp(-1)$ in Eq. (3). However, at low frequencies, the model seems to drop too fast in order to account for the data point at 2.2 GHz.

The Razin-Tsytovitch effect causes the suppression of synchrotron radiation and it occurs when the relativistic electrons are surrounded by plasma. The refractive index of the plasma reduces the Lorentz factors of the electrons which result in a low-frequency cut-off. The frequency of this cut-off is given approximately by $\nu_{\rm RT} = 20 n_e/B$ Hz, where the magnetic field strength B is in units of Gauss and the electron density n_e in cm^{-3}. Thus, the synchrotron emission decreases exponentially below the cut-off frequency, and the spectrum can be approximated using Eq. (3) with $\alpha_{thick} = \alpha_{thin} \sim -0.5$, and $f(\nu) = \exp[-(\nu_{\rm RT}/\nu_0)]/\exp(-1)$. With 10 GHz cut-off frequency, $n_e/B = 5 \times 10^8$. We can estimate the electron number density using the same stellar wind parameters as in Eq. (1) and assume that the radio emission is coming at 1 mas ($r \sim 6 \times 10^{13}$ cm):

$$n_e \approx \frac{\dot{M}\gamma}{4\pi r^2 v_\infty m_H \mu} = 2 \times 10^7 \,\mathrm{cm}^{-3}. \quad (6)$$

Thus, the magnetic field has to be in excess of 0.07 G in order to for the Razin-Tsytovitch effect to take place, which is a reasonable assumption based on the previous estimates.

From the above, we conclude that the synchrotron emission absorbed by the mixed free-free absorption or the Razin-Tsytovitch effect represents best the radio spectrum taken at the

beginning of the minor radio flare. Due to the similar spectral indices obtained at frequencies 4.6–11.2 GHz, this is likely true during the hypersoft state as well.

4.2. Jet quenching

During the hypersoft state, there is clearly radio emission left and opacity is still a factor. However, the radio flux density at least up to 230 GHz is greatly reduced by as much as two orders of magnitude from the baseline/non-flaring state level (similar quenching factors have been observed from other XRBs, e.g., Fender et al. 1999; Russell et al. 2011; Rushton et al. 2016). The spectrum of the quenched radio emission is not optically thin, which would be expected from residual radio lobes. Instead, the spectrum is optically thick with an index close to ∼1, and likely caused by free-free absorption or Razin-Tsytovitch effect (see above). Waltman et al. (1996) discussed that the reduced radio flux densities are unlikely to be absorbed by an enhancement of the WR stellar wind, as the onset of quenched emission should appear later at lower frequencies if the enhanced stellar wind density overtakes the radio photospheres. However, the process of quenching of the radio emission does not appear to have any lag depending on the frequency, thus these authors considered that most likely the mass injection rate to the jet is quenched.

Fender et al. (1997) suggested that during the radio quenched period the mass-loss rate of the WR star increases resulting in an increase of the thermal electron density at the location of the jet, which effectively quenches the jet by a mechanism unknown. At the same time, the infrared emission of the stellar wind is increased owing to higher ion and electron densities. The X-ray emission is also increased as a result of increased mass accretion rate. McCollough et al. (2010) showed that during the soft X-ray state there is a clear brightening (0.3 mag) in the infrared emission in all 2MASS bands. Assuming that the infrared flux comes as a whole from the stellar wind, 0.3 mag brightening correspond to a factor of 1.3 increase in flux, which corresponds to a factor of 1.4 increase in mass-loss rate assuming that $S_\nu \approx \dot{m}^{4/3}$. The infrared flux reaches its maximum during the hypersoft state and the radio flare that follows (McCollough et al. 2010, their Fig. 2). However, it can be also seen that the actual state change started earlier, 10–15 days before the rise in the infrared, when soft X-rays started to increase and hard X-rays began to decrease. If the X-ray spectrum gets softer, the opacity of the wind increases, since there are line/edge absorption processes operating that are not important at the hard X-ray energies. This results in the increase of the wind temperature and subsequently higher infrared radiation. Thus, it seems likely that changes in the accretion flow are driving the quenching rather than changes in the wind mass-loss rate.

Whether the continuum emission comes from the relativistic jet during the hypersoft state is not clear. We cannot exclude a possibility that a weak, self-absorbed jet is still present in the system. However, in the soft states of XRBs, strong disk winds are seen (Neilsen & Lee 2009; Ponti et al. 2012), and these may collide with the WR stellar wind to produce radio emission at the shock front. Systems with colliding stellar winds produce radio emission with luminosities 10^{29}–10^{30} erg/s (De Becker & Raucq 2013) that correspond to a flux density of 1–5 mJy for a distance 7.4 kpc at 5 GHz. The X-ray source could heat the wind even further and lead to a larger flux in free-free emission from the wind.

Furthermore, the correlation of the hard X-ray emission to the radio emission during the hypersoft state hints at a coupling between these emission regions. The coupling can be explained, for example, by a model of Meier (2001), in which the geometrical thickness of the accretion flow is related to its ability to hold a strong poloidal magnetic field. If the hard X-rays are connected either to the base of the jet or the thick accretion flow, then the jet quenching would naturally be correlated with the lack of the hard X-ray emission.

4.3. Origin of the X-ray emission

Zdziarski et al. (2010) showed that the Cyg X–3 spectral energy distribution and the high-frequency power spectra in both soft and hard spectral states can be modeled by assuming that the X-ray source is embedded in a Compton-thick, low-temperature plasma. Compton scattering in the plasma results in a redistribution and isotropisation of the photon spectrum, in such a way that the high-frequency variability of the X-rays is suppressed and the high-energy photons are scattered to lower energies toward the equilibrium temperature of the plasma. The necessary optical depth and equilibrium temperature are however much larger ($\tau \sim 7$, $kT_{\rm bb} \sim 2.5$ keV) than would be expected from the stellar wind alone, and thus they speculated that the interaction of the (focused) stellar wind with the accretion disk would produce a bulge around the compact object with the necessary properties.

The energy spectrum and cospectrum in the hypersoft state support the scattering scenario. We observed strong thermalisation of the incident spectrum, as the hypersoft spectra can be fitted purely with blackbody model. The temperature of the blackbody is lower ($kT_{\rm bb} \sim 1.3$ keV) as compared to the value in Zdziarski et al. (2010), but this obviously depends on the shape of the incident spectrum and the local absorption external to the scattering cloud.

The X-ray cospectrum is a featureless power law spectrum with an index of $\beta = -2.0$, similar to what has been observed previously from the PDS of all accretion states of Cyg X–3 (Axelsson et al. 2009; Koljonen et al. 2011). This differs from what is usually seen from XRBs, which produce flicker noise spectra with flatter index of $\beta \sim -1$ in the soft state (e.g., Gilfanov & Arefiev 2005). The power law PDS with an index $\beta = -2$ usually arises from some kind of red noise process, where high-frequency variations are suppressed (Kylafis & Klimis 1987). It is possible that as the system is enshrouded in a dense stellar wind, the X-ray scattering in the stellar wind results in further suppression of the high-frequency variations mimicking a red noise process. The similarity of the X-ray timing properties in all accretion states implies that the density of the stellar wind stays above a certain density threshold that produces enough X-ray scattering at all times, and the changes in the energy spectrum are due to changes in the accretion process.

Similar X-ray spectral properties as in Cyg X–3 during hypersoft state have been observed in GRO J1655–40 (Uttley & Klein-Wolt 2015; Neilsen et al. 2016; Shidatsu et al. 2016). Uttley & Klein-Wolt (2015) found that during the 2005 outburst the source presented suspiciously similar spectra with Cyg X–3 featuring an absorption edge at $E_{\rm Fe/He} = 8.3$ keV, constant disk temperature of $kT_{\rm bb} = 1.2$ keV, and a Compton scattering fraction of $f_{\rm Comp} = 0.2$. However, the X-ray PDS of GRO J1655–40 does not feature red noise, but has a flat spectrum with a low-frequency cut-off ranging $\nu_{\rm cut} = 0.1 - 10$ Hz. Neilsen et al. (2016) and Shidatsu et al. (2016) argued that the origin of the X-ray spectral and timing properties together with an infrared excess could be explained by a Compton-thick disk wind produced by the accretion disk emitting at or above the Eddington limit. In addition, during the hypersoft state in GRO J1655–40 the radio is also quenched (Migliari et al. 2007). Thus, it could be possible that

Cyg X–3 presents a similar state of super-Eddington accretion in the hypersoft state as in GRO J1655–40 with similar symptoms of soft X-ray spectrum, infrared excess, and radio quenching.

On the other hand, Swift J1753.5–0124 exhibited an unusual spectral state in March–May 2015 with similar properties as the hypersoft state with soft X-ray spectrum and *Swift*/BAT flux consistent with zero (Shaw et al. 2016). At the same, time radio flux was not detected from the source and upper limits with a quenching factor of >25 were obtained (Rushton et al. 2016). However, the X-ray luminosity was shown to be unusually low for a soft state XRB: that is, approximately 0.6% of the Eddington luminosity for a distance of 3 kpc and black hole mass 5 $M_{\odot}$ (Shaw et al. 2016). As the distance is not well established (2–8 kpc; Cadolle Bel et al. 2007; Froning et al. 2014), the Eddington luminosity could be as high as 4%. This indicates that the hypersoft state and jet quenching does not necessarily need Eddington limit accretion rates. In fact, the unabsorbed X-ray luminosity of Cyg X–3 in the hypersoft state ($\sim 10^{38}$ erg/s) indicates ~4–8 % of the Eddington luminosity, which is roughly twice the normal Eddington luminosity as most of the accreted mass is helium, for a black hole accretor of 5–10 $M_{\odot}$. It is unlikely that the hypersoft state in Swift J1753.5–0124 would be a result of a Compton thick wind as the X-ray luminosity is very low to drive a strong disk wind, and the inclination is likely not very high (<55°; Froning et al. 2014). Instead, a Compton-thick disk atmosphere could scatter the accretion disk emission as speculated in Shaw et al. (2016).

Thus, the common theme in these three sources is surprisingly similar: thermal X-ray spectrum with a very weak or non-existent hard X-ray tail coinciding with a very weak or non-existent radio emission. The spectral similarity suggests that the spectral shape is intrinsic to the hypersoft state and is not due to scattering, as these systems have likely different origins and properties of the intervening medium (disk wind, disk atmosphere, and stellar wind). The lack of radio emission in all sources during the hypersoft state suggest that the accretion flow is in a state (not necessarily connected to the Eddington luminosity of the flow) that effectively quenches the jet formation.

4.4. Origin of the γ-ray emission

The detection of γ-ray emission in Cyg X–3 requires an efficient mechanism of producing relativistic particles. This naturally occurs in shocks. The γ-ray emission in Cyg X–3 seems to be usually associated with the hypersoft state (Tavani et al. 2009b; Koljonen et al. 2010). A seemingly strong anticorrelation exists between the γ-ray emission and hard X-ray emission, and it appears that every local minimum in the hard X-ray light curve corresponds to a time when γ-ray emission is detected from the system. The γ-ray flares are usually observed during the declining phase and rising phase to/from the hypersoft state (Tavani et al. 2009b). It is still under debate whether the γ-rays arise from leptonic (Dubus et al. 2010; Zdziarski et al. 2012; Piano et al. 2012) or hadronic processes (e.g., Romero et al. 2003; Piano et al. 2012; Sahakyan et al. 2014). The leptonic scenario is based on the inverse-Compton scattering of soft stellar photons by the relativistic electrons presumably in the jet that is streaming toward us close to the line of sight. The interaction of the jet with the stellar photon field close to the compact object (within ten orbital separations) scatters the photons up to MeV energies. It is also possible that the interaction of the jet with the stellar wind produces a strong recollimation shock in the jet that can lead to strong dissipation of kinetic energy into γ-ray and radio emission (Yoon & Heinz 2015; Yoon et al. 2016). In addition, clumps in the stellar wind can enhance the production of shocks and subsequently the γ-ray emission (de la Cita et al. 2017). The hadronic scenario, in which the jet would be populated with protons, is based on the proton-proton collisions that occur between the protons in the hadronic jet and protons in the stellar wind. The collisions produce pions and γ-rays via the decay of neutral pions.

However, γ-rays have also been detected outside of major radio flare episodes and have been associated with very brief periods of hard X-ray quenching and minor radio flaring (Corbel et al. 2012; Bulgarelli et al. 2012). In one case the hard X-ray quenching lasted only ~0.5 days and in the other case, this quenching lasted for a day. Interestingly, γ-rays are also reported to occur without associated enhancement of the radio emission (Williams et al. 2011) and/or hard X-ray quenching (Bodaghee et al. 2013). Thus, the jet origin of the γ-rays is still debatable as both Williams et al. (2011) and Bodaghee et al. (2013) presented some evidence against the model of inverse-Compton scattering of soft stellar photons by the jet.

We note briefly here that if Cyg X–3 exhibits strong disk wind similar to GRO J1655–40, its collision with the stellar wind may be strong enough to provide some or all of the γ-rays from Cyg X–3. Overall, the γ-ray luminosity is a factor of about 100 larger than that from the colliding wind binary η Carinae (Abdo et al. 2010). The mass-loss rates and velocities of the winds of the two systems are very similar. The density at the shock interface in Cyg X–3 should be much larger, resulting from smaller orbital separation. A detailed study of this possibility is out of the scope of this work, but it appears to be a viable possibility that the disk wind and stellar wind interaction may supply at least some of the γ-ray power in Cyg X–3.

4.5. The proposed scenario

In order to tie together all the above phenomena observed from Cyg X–3, we propose the following scenario that expands on those presented in Fender et al. (1997) and Vadawale et al. (2003). In the former, the thermal electron density in the vicinity of the compact object increases, because of increased mass-loss from the WR companion, and quenches the jet launching mechanism. The increased mass-loss results in the increase of the mass accretion rate to the compact object, which eventually leads to a large injection of matter into the jet. Because of the higher thermal electron density, the relativistic particles in the jet are mixed with a high proportion of absorbing thermal electrons producing opacity to the synchrotron emission. As the mass-loss rate decreases with time, the opacity also decreases in the radio flares. The scenario in Vadawale et al. (2003) is based on the internal shock model (Rees 1978; Marscher & Gear 1985; Kaiser et al. 2000), where the traveling plasmons in the jet are associated with shocks that arise from the differential velocity of the moving jet material. Considering the case of GRS 1915+105, these authors presented a model where during a hard-to-soft state transition unstable accretion flow changes result in discrete, multiple ejections of matter in the jet that collide with the continuous, flat spectrum jet that is present in XRBs during the hard state and produce shocks and episodic radio flares. On the other hand, during the soft state, the jet is quenched, and the reignition of the jet when the source transits from the soft state back to the hard state does not result in shock formation and subsequent radio flaring as there is not material present for the jet to collide with.

We posit that the work surface for the jet can be either the stellar wind or the continuous, flat spectrum jet. Thus, we develop a scenario in which systems with strong stellar winds should see more powerful radio episodes at the transitions from soft states to hard states than at the transitions from hard states to soft states. In the hard state, a jet constantly works against the stellar wind in the system, evacuating a cocoon in a similar fashion as the jets in SS 433 (e.g., Fabrika 2004) and ultraluminous XRBs (e.g., Pakull et al. 2010). It is possible that the formation of a strong recollimation shock in the jet (Yoon & Heinz 2015; Yoon et al. 2016) enhances the radio emission to levels above normal, persistent XRB, which exhibit radio flux densities below 20 mJy with smaller distances (Fender & Hendry 2000). Because of changes in the accretion flow, the accretion rate to the compact object increases resulting in higher soft X-ray luminosity and higher infrared luminosity as discussed above. As the source descends to the hypersoft state, the jet quenches after producing episodic shocks similar to other XRBs when transiting to the soft state. When these shocks interact with the stellar wind (or possibly with the clumps in the wind; de la Cita et al. 2017), they produce γ-ray emission. During the time that the jet stays quenched, the stellar wind is able to fill the cocoon region back in. When the source makes a transition back to the hard state, the jet turns back on and it encounters a medium with the density of the stellar wind. This medium is far denser than the relativistic jet would normally be and is also essentially at rest relative to the fast jet (i.e., it moves at a speed a factor of about 100 slower). This interaction leads to efficient shock production in the jet and radio and γ-ray emission (Yoon & Heinz 2015; Yoon et al. 2016). The thermal matter of the stellar wind is entrained in the jet producing increased opacity of the synchrotron radiation until the cocoon is blown again by the jet pressure. A cartoon of this paradigm is presented in Fig. 13.

It has often been stated that the jets turn off in the soft states of black hole XRBs simply because the radio emission turns off. An alternative, in principle, is that the radiative efficiency drops in the jet (e.g., "dark jets" in soft states, Drappeau et al. 2017; or Poynting flux dominated jets, e.g., Sikora et al. 2005) or that the jet Lorentz factors become sufficiently large that observers sitting outside the beaming cone simply do not detect flux from these jets (Maccarone 2005). The scenario we propose here strengthens the evidence for the idea that the jets really do turn off or become very weak in the soft state. If the jets remained on with a similar jet power as in the hard state, then there would remain an evacuated cavity in the stellar wind from the donor star of Cyg X–3 even during the soft state, and the radio power upon returning to the hard state would not be dramatically higher than at the hard-to-soft transition. It seems unlikely that a Poynting flux dominated jet could travel through such a large amount of material without depositing energy, but a detailed calculation of this scenario does not exist in the literature.

In recent years, a controversy has developed surrounding whether it can be demonstrated that black hole spin has an important effect on the jet properties (e.g., Narayan & McClintock 2012; Russell et al. 2013; Koljonen et al. 2015). In most cases, the radio luminosity of the jet is used as a proxy for its kinetic power, although in some cases, with careful modeling, the kinetic power of jet can be estimated from the jet-interstellar medium interactions (Gallo et al. 2005; Russell et al. 2007; Cooke et al. 2007; Sell et al. 2015). The latter approach is frequently used in AGN studies because of concerns about the effects of beaming if core radio fluxes are used. Low-mass XRBs show strong hysteresis effects in their state transition luminosities, as this has been found both for black hole systems (Miyamoto et al. 1995) and neutron star systems (Maccarone & Coppi 2003). This means that the hard-to-soft state transitions for the low-mass XRBs, in addition to having denser media for internal shocking than the jets produced at the soft-to-hard transition, these objects also have higher X-ray luminosities at the transition and likely higher kinetic powers apart from any spin effects. Cyg X–3, like Cyg X-1, does not show hysteresis effects in its state transitions, probably because its outer disk radius, as a wind-fed system, is small enough that it is not a bona fide transient in X-rays (e.g., Smith et al. 2002). Thus, differences in the accretion luminosity cannot be used to explain the differences in jet radio luminosity; they must come from either a difference in how accretion power is converted into jet power, or how the jet power is dissipated and converted into radio emission.

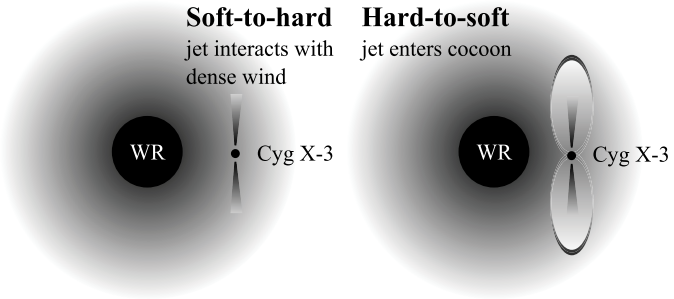

Fig. 13. Cartoon of the jet-wind interaction for Cyg X–3. *Left:* in the hypersoft state the jet is turned off and the stellar wind is allowed to expand freely close to the compact object. When the jet turns back on during the state transition, it encounters a dense medium at rest relative to the jet which leads to efficient shock production and subsequently to strong radio and γ-ray emission. *Right:* when Cyg X–3 is transiting from the hard state to the hypersoft state, the hard state compact jet has blown out a cocoon in the stellar wind, into which the episodic jet can then expand more freely producing weaker radio emission than when expanding directly into a stellar wind. We note that the stellar sizes and the binary separation are not to scale with respect to the jet.

Our explanation for the behavior of Cyg X–3, as coming from the very dense medium in which the jet kinetic power is dissipated, rather than from the differences in kinetic power itself, thus has implications for all attempts to estimate the kinetic power of transient jets based on radio flux. It is likely that the spread of variation in the densities of ambient media around low-mass XRBs is substantially smaller than the difference between these typical values and the density of the stellar wind around Cyg X–3, but this remains a potential error source that is not well discussed in the current literature.

5. Conclusions

We have studied the multiwavelength properties of Cyg X–3 during the hypersoft state that is observed prior to major outburst events and jet ejection episodes. We have shown that the radio/sub-mm emission is diminished by two orders of magnitudes and present the lowest radio flux densities in the source evolution. The radio emission size region is the most compact in the source evolution, however, it is much larger than the orbital separation of the binary. The radio emission in low frequencies during the hypersoft state (and in the beginning of radio flares) is likely absorbed by thermal plasma mixed with the non-thermal electron population. We have also suggested that the

residual radio emission in the hypersoft state could arise from the wind-wind interaction of the binary and not from the jet.

We have shown that the broadband X-ray spectrum is consistent with a thermal, absorbed blackbody emission and a Comptonized component from a population of high-energy electrons that are moving or changing the subtended angle as viewed from the seed photon population in ksec timescales. The radio emission was also found to be coupled to the hard X-ray emission at the same timescale. The X-ray spectra are subjected to absorption and electron scattering by the stellar wind, which seems to be manifest in all accretion states. Thus, the accretion state change to/from the hypersoft state is linked to changes in the accretion flow and not in the stellar wind structure.

Cyg X–3 is an XRB that shows the standard spectral state transition phenomenology of XRBs but shows a different jet radio power phenomenology. We have shown that a coherent picture of the behavior of the system can be developed if one considers the effects of the stellar wind on the radio emission and of the jet on the stellar wind density. In the hard state, the jet constantly evacuates a cocoon in the stellar wind, while in the hypersoft state, the wind refills this region, providing a work surface for the jet when the disk returns to the hard state. Our scenario, in particular, provides evidence that the jets are actually quenched in the soft states, rather than becoming radiatively inefficient or traveling with very high Lorentz factors such that the flux outside the beaming cone is strongly deboosted.

Acknowledgements. The Submillimeter Array is a joint project between the Smithsonian Astrophysical Observatory and the Academia Sinica Institute of Astronomy and Astrophysics and is funded by the Smithsonian Institution and the Academia Sinica. *Swift*/BAT transient monitor results are provided by the *Swift*/BAT team. This research has made use of MAXI data provided by RIKEN, JAXA, and the MAXI team. TSA acknowledges support through the Russian Government Program of Competitive Growth of Kazan Federal University. We thank Sebastian Heinz and Chris Fragile for useful discussions.

References

Abdo A. A et al. (Fermi LAT Collaboration),2009, Science, 326, 1512
Abdo, A. A., Ackermann, M., Ajello, M., et al. 2010, ApJ, 723, 649
Axelsson, M., Larsson, S., & Hjalmarsdotter, L. 2009, MNRAS, 394, 1544
Bachetti, M. 2015, MaLTPyNT: Quick look timing analysis for NuSTAR data, Astrophysics Source Code Library
Bachetti, M., Harrison, F. A., Cook, R., et al. 2015, ApJ, 800, 109
Barbiellini, G., Fedel, G., Liello, F., et al. 2002, Nucl. Instr. Meth. Phys. Res. B, 490, 146
Beckmann, V., Soldi, S., Bélanger, G., et al. 2007, A&A, 473, 903
Bodaghee, A., Tomsick, J. A., Pottschmidt, K., et al. 2013, ApJ, 775, 98
Bulgarelli, A., Tavani, M., Chen, A. W., et al. 2012, A&A, 538, A63
Burrows, D. N., Hill, J. E., Nousek, J. A., et al. 2005, Space Sci. Rev., 120, 165
Cadolle Bel, M., Ribó, M., Rodriguez, J., et al. 2007, ApJ, 659, 549
Cheung, C. C., & Loh, A. 2016, ATel, 9502
Cooke, R., Kuncic, Z., Sharp, R., & Bland-Hawthorn, J. 2007, ApJ, 667, L163
Corbel, S., Dubus, G., Tomsick, J. A., et al. 2012, MNRAS, 421, 2947
De Becker, M., & Raucq, F. 2013, A&A, 558, A28
de la Cita, V. M., del Palacio, S., Bosch-Ramon, V., et al. 2017, A&A, 604, A39
Dickey, J. M., & Lockman, F. J. 1990, ARA&A, 28, 215
Drappeau, S., Malzac, J., Coriat, M., et al. 2017, MNRAS, 466, 4272
Dubus, G., Cerutti, B., & Henri, G. 2010, MNRAS, 404, L55
Earnshaw, H. M., & Roberts, T. P. 2017, MNRAS, 467, 2690
Egron, E., Pellizzoni, A., Giroletti, M., et al. 2017, MNRAS, 471, 2703
Fabrika, S. 2004, Astrophys. Space Phys. Rev., 12, 1
Fender, R., Corbel, S., Tzioumis, T., et al. 1999, ApJ, 519, L165
Fender, R. P., & Hendry, M. A. 2000, MNRAS, 317, 1
Fender, R. P., Bell Burnell, S. J., Garrington, S. T., Spencer, R. E., & Pooley, G. G. 1995, MNRAS, 274, 633
Fender, R. P., Bell Burnell, S. J., Waltman, E. B., et al. 1997, MNRAS, 288, 849
Froning, C. S., Maccarone, T. J., France, K., et al. 2014, ApJ, 780, 48
Gallo, E., Fender, R., Kaiser, C., et al. 2005, Nature, 436, 819
Gehrels, N., Chincarini, G., Giommi, P., et al. 2004, ApJ, 611, 1005
Gilfanov, M., & Arefiev, V. 2005, ArXiv Astrophysics [arXiv: astro-ph/0501215]
Gregory, P. C., & Seaquist, E. R. 1974, ApJ, 194, 715
Harrison, F. A., Craig, W. W., Christensen, F. E., et al. 2013, ApJ, 770, 103
Hjalmarsdotter, L., Zdziarski, A. A., Larsson, S., et al. 2008, MNRAS, 384, 278
Hornby, J. M., & refauWilliams, P. J. S. 1966, MNRAS, 131, 237
Kaiser, C. R., Sunyaev, R., & Spruit, H. C. 2000, A&A, 356, 975
Kallman, T. R., Palmeri, P., Bautista, M. A., Mendoza, C., & Krolik, J. H. 2004, ApJS, 155, 675
Kellermann, K. I.,, & Pauliny-Toth, I. I. K. 1981, ARA&A, 19, 373
Koljonen, K. I. I., & Maccarone, T. J. 2017, MNRAS, 472, 2181
Koljonen, K. I. I., Hannikainen, D. C., McCollough, M. L., Pooley, G. G., & Trushkin, S. A. 2010, MNRAS, 406, 307
Koljonen, K. I. I., Hannikainen, D. C., & McCollough, M. L. 2011, MNRAS, 416, L84
Koljonen, K. I. I., McCollough, M. L., Hannikainen, D. C., & Droulans, R. 2013, MNRAS, 429, 1173
Koljonen, K. I. I., Russell, D. M., Fernández-Ontiveros, J. A., et al. 2015, ApJ, 814, 139
Krimm, H. A., Holland, S. T., Corbet, R. H. D., et al. 2013, ApJS, 209, 14
Kylafis, N. D., & Klimis, G. S. 1987, ApJ, 323, 678
Leitherer, C., & Robert, C. 1991, ApJ, 377, 629
Lindfors, E. J., Türler, M., Hannikainen, D. C., et al. 2007, A&A, 473, 923
Loh, A., & Corbel, S. 2017a, ATel, 10109
Loh, A., & Corbel, S. 2017b, ATel, 10243
Maccarone, T. J. 2005, MNRAS, 360, L68
Maccarone, T. J., & Coppi, P. S. 2003, MNRAS, 338, 189
Marscher, A. P., & Gear, W. K. 1985, ApJ, 298, 114
Marti, J., Paredes, J. M., & Estalella, R. 1992, A&A, 258, 309
Matsuoka, M., Kawasaki, K., Ueno, S., et al. 2009, PASJ, 61, 999
McCollough, M., Koljonen, K., Hannikainen, D., et al. 2010, in The Restless Gamma-ray Universe (INTEGRAL 2010), Eighth Integral Workshop, 25
McCollough, M. L., Robinson, C. R., Zhang, S. N., et al. 1999, ApJ, 517, 951
McCollough, M. L., Corrales, L., & Dunham, M. M. 2016, ApJ, 830, L36
Meier, D. L. 2001, ApJ, 548, L9
Migliari, S., Tomsick, J. A., Markoff, S., et al. 2007, ApJ, 670, 610
Mihara, T., Nakajima, M., Sugizaki, M., et al. 2011, PASJ, 63, S623
Miller, J. M., Raymond, J., Reynolds, C. S., et al. 2008, ApJ, 680, 1359
Miller-Jones, J. C. A., Blundell, K. M., Rupen, M. P., et al. 2004, ApJ, 600, 368
Miller-Jones, J. C. A., Sakari, C. M., Dhawan, V., et al. 2009, in 8th Int. e-VLBI Workshop, 17
Mioduszewski, A. J., Rupen, M. P., Hjellming, R. M., Pooley, G. G., & Waltman, E. B. 2001, ApJ, 553, 766
Miyamoto, S., Kitamoto, S., Hayashida, K., & Egoshi, W. 1995, ApJ, 442, L13
Narayan, R. & McClintock, J. E. 2012, MNRAS, 419, L69
Neilsen, J., & Homan, J. 2012, ApJ, 750, 27
Neilsen, J., & Lee, J. C. 2009, Nature, 458, 481
Neilsen, J., Rahoui, F., Homan, J., & Buxton, M. 2016, ApJ, 822, 20
Ogley, R. N., Bell Burnell, S. J., Spencer, R. E., et al. 2001, MNRAS, 326, 349
Orosz, J. A., & Bailyn, C. D. 1997, ApJ, 477, 876
Paerels, F., Cottam, J., Sako, M., et al. 2000, ApJ, 533, L135
Pakull, M. W., Soria, R., & Motch, C. 2010, Nature, 466, 209
Piano, G., Tavani, M., Vittorini, V., et al. 2012, A&A, 545, A110
Piano, G., Tavani, M., Bulgarelli, A., et al. 2016, ATel, 9429
Piano, G., Tavani, M., Munar-Adrover, P., et al. 2017a, ATel, 10138
Piano, G., Tavani, M., Verrecchia, F., et al. 2017b, ATel, 10179
Ponti, G., Fender, R. P., Begelman, M. C., et al. 2012, MNRAS, 422, L11
Prest, M., Barbiellini, G., Bordignon, G., et al. 2003, Nucl. Instrum. Methods Phys. Res. A, 501, 280
Rees, M. J. 1978, MNRAS, 184, 61P
Romero, G. E., Torres, D. F., Kaufman Bernadó, M. M., & Mirabel, I. F. 2003, A&A, 410, L1
Rushton, A. P., Shaw, A. W., Fender, R. P., et al. 2016, MNRAS, 463, 628
Russell, D. M., Fender, R. P., Gallo, E., & Kaiser, C. R. 2007, MNRAS, 376, 1341
Russell, D. M., Gallo, E., & Fender, R. P. 2013, MNRAS, 431, 405
Russell, D. M., Miller-Jones, J. C. A., Maccarone, T. J., et al. 2011, ApJ, 739, L19
Sahakyan, N., Piano, G., & Tavani, M. 2014, ApJ, 780, 29
Savolainen, P. 2012, in X-ray Binaries. Celebrating 50 Years Since the Discovery of Sco X–1, 52
Sell, P. H., Heinz, S., Richards, E., et al. 2015, MNRAS, 446, 3579
Shaw, A. W., Gandhi, P., Altamirano, D., et al. 2016, MNRAS, 458, 1636
Shidatsu, M., Done, C., & Ueda, Y. 2016, ApJ, 823, 159
Sikora, M., Begelman, M. C., Madejski, G. M., & Lasota, J.-P. 2005, ApJ, 625, 72
Simon, M. 1969, ApJ, 156, 341

Sincell, M. W., & Krolik, J. H. 1994, ApJ, 430, 550
Smale, A. P., Mushotzky, R. F., Schlegel, E. M., et al. 1993, ApJ, 418, 894
Smith, D. M., Heindl, W. A., & Swank, J. H. 2002, ApJ, 569, 362
Steiner, J. F., Narayan, R., McClintock, J. E., & Ebisawa, K. 2009, PASP, 121, 1279
Szostek, A. & Zdziarski, A. A. 2005, in X-ray Diagnostics of Astrophysical Plasmas: Theory, Experiment, and Observation, ed. R. Smith, AIP Conf. Ser., 774, 341
Szostek, A., & Zdziarski, A. A. 2008, MNRAS, 386, 593
Szostek, A., Zdziarski, A. A., & McCollough, M. L. 2008, MNRAS, 388, 1001
Tavani, M., Barbiellini, G., Argan, A., et al. 2009a, A&A, 502, 995
Tavani, M., Bulgarelli, A., Piano, G., et al. 2009b, Nature, 462, 620
Trushkin, S., McCollough, M., Nizhelskij, N., & Tsybulev, P. 2017a, Galaxies, 5, 86
Trushkin, S. A., Nizhelskij, N. A., Tsybulev, P. G., & Zhekanis, G. V. 2017b, in Stars: From Collapse to Collapse, eds. Y. Y. Balega, D. O. Kudryavtsev, I. I. Romanyuk, & I. A. Yakunin, in ASP Conf. Ser., 510, 492
Tudose, V., Fender, R. P., Garrett, M. A., et al. 2007, MNRAS, 375, L11
Uttley, P., & Klein-Wolt, M. 2015, MNRAS, 451, 475
Vadawale, S. V., Rao, A. R., Naik, S., et al. 2003, ApJ, 597, 1023
van der Laan, H. 1966, Nature, 211, 1131
van Kerkwijk, M. H., Charles, P. A., Geballe, T. R., et al. 1992, Nature, 355, 703
Vaughan, S., Edelson, R., Warwick, R. S., & Uttley, P. 2003, MNRAS, 345, 1271
Vilhu, O., Hakala, P., Hannikainen, D. C., McCollough, M., & Koljonen, K. 2009, A&A, 501, 679
Waltman, E. B., Fiedler, R. L., Johnston, K. J., & Ghigo, F. D. 1994, AJ, 108, 179
Waltman, E. B., Foster, R. S., Pooley, G. G., Fender, R. P., & Ghigo, F. D. 1996, AJ, 112, 2690
Williams, P. K. G., Tomsick, J. A., Bodaghee, A., et al. 2011, ApJ, 733, L20
Wright, A. E., & Barlow, M. J. 1975, MNRAS, 170, 41
Yoon, D., & Heinz, S. 2015, ApJ, 801, 55
Yoon, D., Zdziarski, A. A., & Heinz, S. 2016, MNRAS, 456, 3638
Zdziarski, A. A., Misra, R., & Gierliński, M. 2010, MNRAS, 402, 767
Zdziarski, A. A., Sikora, M., Dubus, G., et al. 2012, MNRAS, 421, 2956
Zwart, J. T. L., Barker, R. W., Biddulph, P., et al. 2008, MNRAS, 391, 1545